Hindawi
International Journal of Aerospace Engineering
Volume 2022, Article ID 6215047, 22 pages
https://doi.org/10.1155/2022/6215047

Research Article

The Limitation Analysis of Two Dimensional Magnetic Field Configuration in Annular Ion Thruster

Guangqing Xia,[1,2,3] Ziping Wang,[1] Chang Lu ,[1,2,3] and Bin Sun[1]

[1]*State Key Laboratory of Structural Analysis for Industrial Equipment, Dalian University of Technology, Dalian 116024, China*
[2]*Key Laboratory of Advanced Technology for Aerospace Vehicles of Liaoning Province, Dalian University of Technology, Dalian 116024, China*
[3]*Key Laboratory of Trans-Media Aerial Underwater Vehicle of Hebei Province, North China Institute of Aerospace Engineering, Langfang 065000, China*

Correspondence should be addressed to Chang Lu; changlu@dlut.edu.cn

Received 13 February 2022; Accepted 28 March 2022; Published 21 April 2022

Academic Editor: Angelo Cervone

In this paper, the limitations of two-dimensional magnetic field configuration for an annular ion thruster are analyzed theoretically and numerically. The two-dimensional magnetic field, which is commonly used in traditional ion thrusters, has been proved to be a very effective way for the confinement of primary electrons and ions. Hence, the confinement characteristics of primary electrons and ions in an annular ion thruster with the two-dimensional magnetic field configuration are first analyzed theoretically. Then, according to the analysis, a two-dimensional magnetic field for an annular ion thruster is designed. On this basis, the limitations of the two-dimensional magnetic field configuration are analyzed and discussed by a three-dimensional (3D) Particle-in-cell Monte Carlo collision (PIC-MCC) model. The results show that if the collision process is not considered, a uniform distribution of primary electrons can be achieved theoretically. However, when considering the collision process, the atom forms a significant impedance to the circumferential motion of primary electrons, thus greatly increasing the loss rate of primary electrons. Finally, it is found that, since primary electrons are not guided and constrained in the circumferential direction under the two-dimensional magnetic field, the discharge uniformity cannot be improved only by increasing the magnetic field intensity.

1. Introduction

Due to significant advantages, electric propulsion has been widely used in scientific and commercial space missions [1–4]. As one of the most widely used electric propulsions, conventional Kaufman-type ion thruster has successfully carried out many space missions due to its high efficiency and specific impulse [5–7]. To further improve its thrust and power to cope with the next deep space exploration, Patterson and Herman [8] proposed a new kind of Kaufman-type ion thruster, i.e., the annular ion thruster [9–11]. The newly proposed annular ion thruster utilizes the double annular anodes design which makes its ion optics easily manufactured. Meanwhile, since the area of anode increase nearly doubled, its input power can increase greatly [12, 13]. However, the cathode of annular ion thruster biases on the one side of the discharge chamber, making its discharge process uneven. This is very harmful to ion optics and can lead to excessive discharge loss [14]. Therefore, how to keep a uniform discharge is quite critical for the application of annular ion thruster [15].

In Kaufman-type ion thruster, the magnetic field is one of the most important parameters for performance. The magnetic field is produced by the permanent magnets off anodes and used to confine primary electrons and plasma. In a well-designed magnetic field, most electrons (including primary electrons and secondary electrons in plasma) will be constrained and lost only at the magnetic tip, while most ions will be extracted by ion optics [16]. Since electrons have a small loss area, they can have a long average confinement

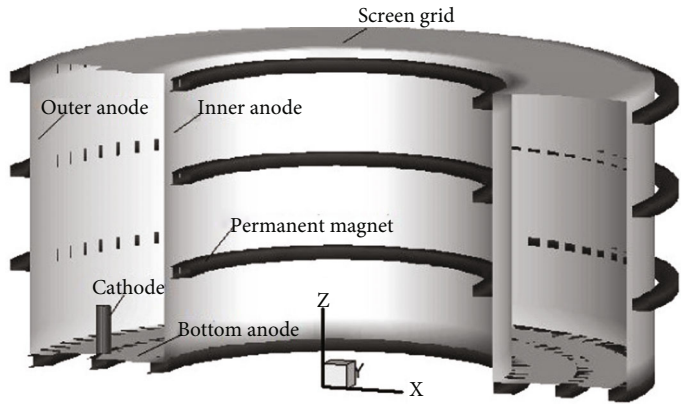

Figure 1: Structure diagram of annular ion thruster.

Table 1: The geometric parameters.

Parameter	Value (unit m)
Outer anode diameter r_o	0.045
Height of outer anode	0.216
Inner anode diameter r_i	0.135
Height of inner anode	0.216
Radius of cathode	0.012
Height of cathode	0.036

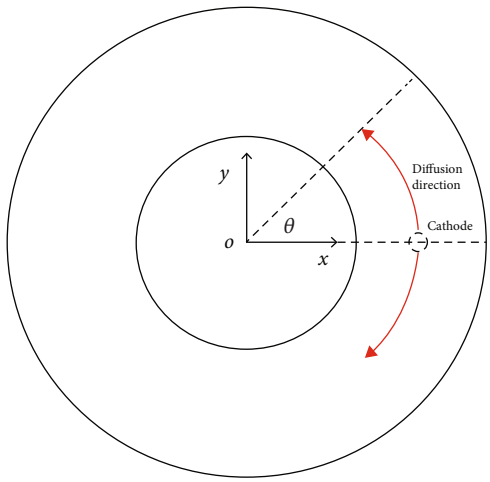

Figure 2: Structure diagram of circumferential diffusion.

length, which makes them uniformly distributed in the discharge chamber. Also, since most ions can be used to produce the thrust, the discharge loss is small. Hence, an excellent magnetic field structure can greatly improve the uniformity of primary electrons and improve other performance of the Kaufman-type ion thruster.

Due to the success of the two-dimensional magnetic field configuration which is commonly used in conventional Kaufman-type ion thruster, in current designs, the two-dimensional magnetic field configuration is also adopted in annular ion thruster. However, under this design, serious nonuniform discharge was also observed [17]. Due to the nonaxisymmetric, it is difficult for the plasma to diffuse uniformly in the discharge chamber. Most plasma mainly concentrates on the cathode side, leading to quite high discharge loss. This means that it may not be suitable to use the two-dimensional magnetic field configuration directly in the annular ion thruster.

Therefore, to better understand the limitations of two-dimensional magnetic field configuration when it is used for the annular ion thruster, its characteristics are analyzed in this paper. First, the confinement characteristics of primary electrons and ions in an annular ion thruster with the two-dimensional magnetic field configuration are analyzed theoretically. Then according to the analysis, a two-dimensional magnetic field for the annular ion thruster is designed and presented. After that, the limitations of the two-dimensional magnetic field configuration are analyzed and discussed by a three-dimensional (3D) Particle-in-cell Monte Carlo collision (PIC-MCC) model. Section 2 presents the confinement characteristics of primary electrons and ions by theoretical analysis. The designed two-dimensional magnetic field is also presented. In Section 3, the 3D PIC-MCC model is presented. Then, the simulation results and the analysis are provided. Finally, the conclusions will be given in Section 4.

2. Theoretical Analysis of Magnetic Confinement of Charged Particles

In this section, the radial and axial distributions of primary electrons and ions are analyzed theoretically. Then, the basic design criteria of the two-dimensional magnetic field configuration and the designed magnetic field for an annular ion thruster will be given according to the theoretical analysis results.

2.1. Distribution Characteristics of Primary Electrons. Figure 1 shows the schematic diagram of an annular ion thruster. It mainly consists of five parts: inner anode, outer anode, bottom anode, cathode, permanent magnet, and ion optics. In Figure 1, the settings of several permanent magnets are just schematic. Table 1 shows the relevant geometric parameters.

Table 2: The case group setting for circumferential distribution of primary electrons.

Parameter	Case group 1	Case group 2	Case group 3	Case group 4
$B(T)$	0.05, 0.1, 0.15, 0.2, 0.25, 0.3	0.2	0.2	0.2
N	9	1, 6, 11, 16, 21, 26	9	9
$\Delta r(m)$	0.121	0.121	0.05035, 0.06448, 0.07861, 0.09274, 0.10687, 0.121	0.121
$H(m)$	0.24	0.24	0.24	0.168, 0.1824, 0.1968, 0.2112, 0.2256, 0.24
$\sum_j^N 2r_j r_p\left(10^{-4}m^{-2}\right)$	11.0, 5.5325, 3.6883, 2.7662, 2.213, 1.8442	0.34578, 2.0747, 3.8036, 5.5325, 7.2614, 8.9903	2.2516, 2.3545, 2.4574, 2.5604, 2.6633, 2.7662	2.7662

In discharge chamber, the primary electrons will be first injected from the hollow cathode. Meanwhile, for the primary electrons, the discharge chamber can be regarded as a space with a reflection boundary. Primary electrons are mainly lost near the tip of the magnetic line perpendicular to the wall. The primary electrons move back and forth along the discharge chamber until they collide with the anode in the effective contact area near the magnetic tip, either by ionization or excitation collision with a neutral gas, or heated by Coulomb interaction with plasma electrons. According to the above characteristics, we try to figure out the circumferential and axial distribution of primary electrons theoretically.

2.1.1. Circumferential Distribution Characteristics of Primary Electrons. First, ignoring the impact of collisions on the motion of the primary electron, the primary electron only loses at the tip of the magnetic field. The loss area at one magnet tip is defined as

$$A_p^i = 2r_p L_m^i = \frac{2}{\|B_i\|}\sqrt{\frac{2m_p v_p T_p}{q_p}} L_m^i, \tag{1}$$

where A_p^i is the loss area at the i_{th} magnet tip, L_m^i is the length of the i_{th} magnet, B_i is the magnetic field intensity at the i_{th} magnet tip, and T_p is the electron temperature in eV.

Suppose there are N permanent magnets, then the primary electron current lost at the tip of the magnetic field is equal to

$$I_p = n_p q_p v_p A_p, \tag{2}$$

where

$$A_p = \sum_i^N A_p^i. \tag{3}$$

The primary electron density distribution satisfies the continuity rule,

$$\frac{dn_p}{dt} + \nabla\left(n_p u_p\right) = G - L, \tag{4}$$

where n_p is the primary electron density, t is time, u_p is the diffusion velocity of primary electrons, G is the generation rate of primary electrons, and L is the loss rate of primary electrons.

As shown in Figure 2, it is assumed that the entry of primary electrons is regarded as the boundary condition, i.e., $G = 0$, while their loss at the tip of the magnetic field can be regarded as a spatial loss rate, i.e., L. Assuming that the primary electrons are uniformly distributed in the radial and axial directions, we can simplify Eq. (4) into a one-dimensional equation with the variable θ.

Ignoring the radial and axial variations of the primary electron density, in polar coordinates, Eq. (4) can be rewritten as

$$\frac{dn_p}{dt} + \frac{1}{r}\frac{d\left(n_p u_p^\theta\right)}{d\theta} = G - L, \tag{5}$$

where r is the compromise radius, $r = 1/2(r_o + r_i)$, r_o is the outer radius, and r_i is the inner radius; u_p^θ is the circumferential diffusion velocity of primary electrons.

L can be expressed as

$$L = \frac{I_p}{q_p A_P}\frac{\sum_j^N 2r_j r_p}{1/2\left(r_o^2 - r_i^2\right)H}, \tag{6}$$

where r_j is the radius of the j_{th} magnet, and H is the height of the thruster discharge chamber.

In steady-state, this one-dimensional equation can be expressed as

$$\frac{d\left(n_p u_p^\theta\right)}{d\theta}(r_o - r_i)H = -\frac{I_p}{q_p A_p}\sum_j^N 2r_j r_p. \tag{7}$$

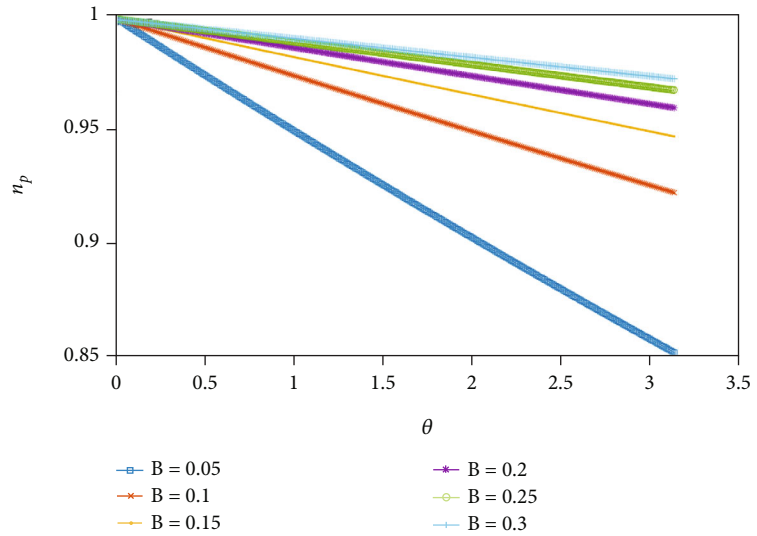

(a) Under different magnetic induction intensity

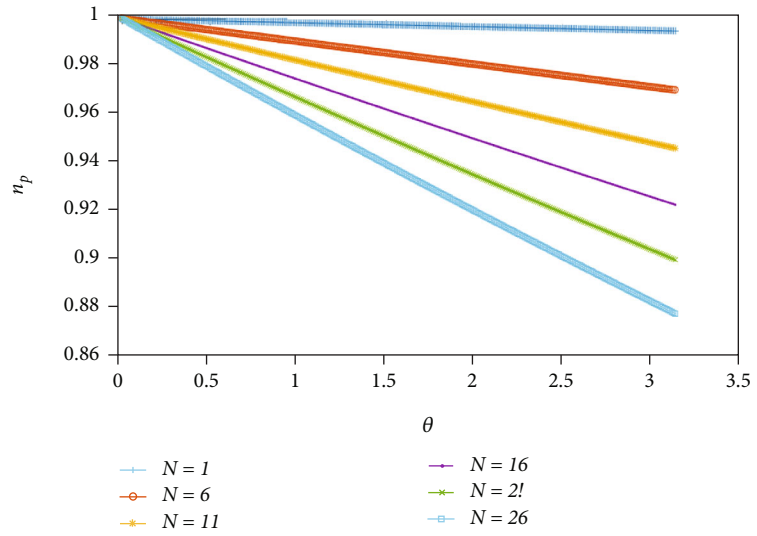

(b) Under different numbers of permanent magnets

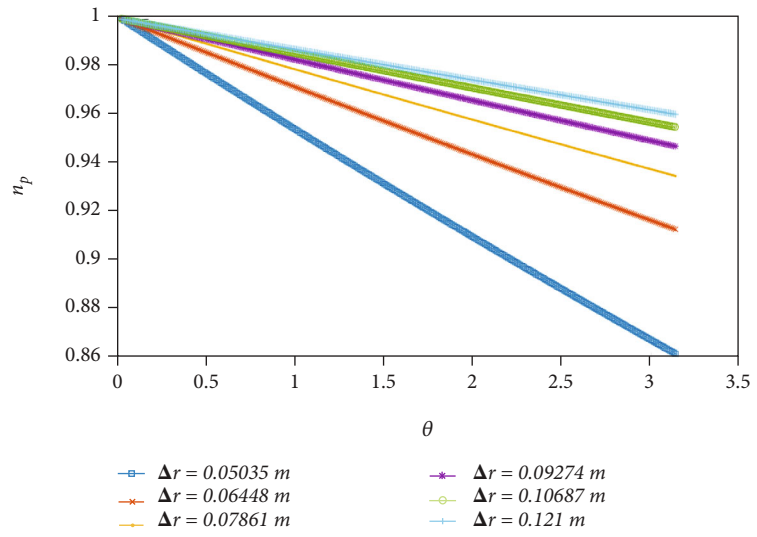

(c) Under different channel widths

Figure 3: Continued.

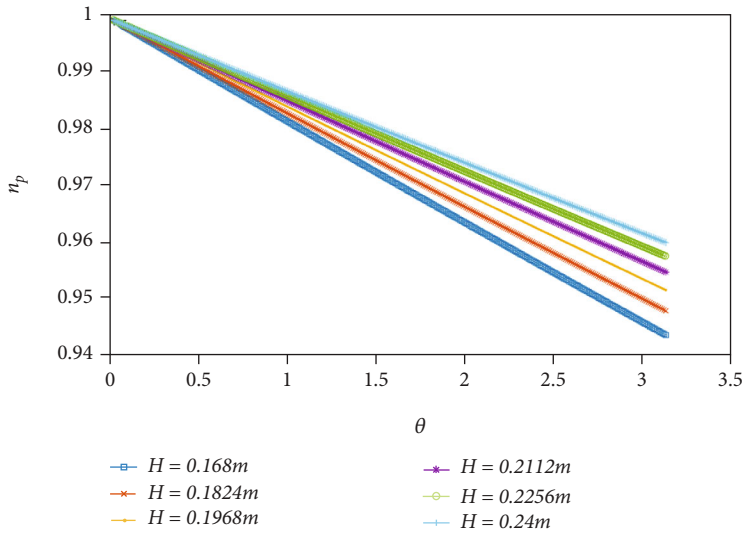

(d) Under different channel heights

Figure 3: Variation of primary electron density under different parameters.

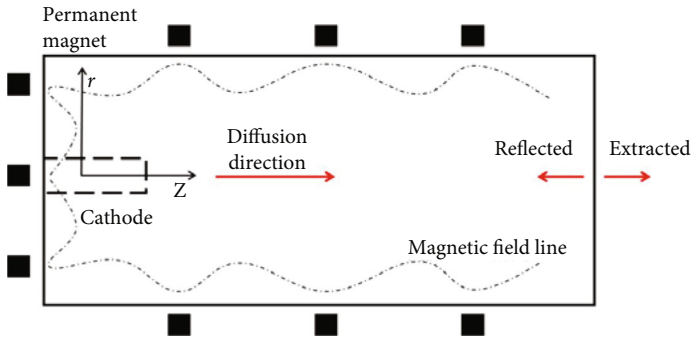

Figure 4: Structure diagram of radial diffusion.

Table 3: The case group setting for axis distribution of primary electrons.

Parameter	Case group 5	Case group 6	Case group 7
$B(T)$	0.05, 0.1, 0.15, 0.2, 0.25, 0.3	0.2	0.2
N	9	1, 6, 11, 16, 21, 26	9
$\Delta r(m)$	0.121	0.121	0.05035, 0.06448, 0.07861, 0.09274, 0.10687, 0.121
$A_s(m)$	0.1082	0.1082	0.0193, 0.0346, 0.0511, 0.0689, 0.0879, 0.1082
$\sum_i^N L_m^i(m)$	9.4097	1.1762, 7.0573, 12.9383, 18.8194, 24.7005, 30.5815	7.659, 8.0091, 8.3593, 8.7094, 9.0595, 9.4097

If the collision process is ignored, u_p^θ can be regarded as constant and $u_p^\theta \approx v_p$, then, we can get

$$\frac{dn_p}{d\theta} = -n_p \frac{\sum_j^N 2r_j r_p}{(r_o - r_i)H}. \tag{8}$$

Finally, we can obtain the circumferential distribution of the primary electrons as follows

$$n_p = n_p^0 e^{-\theta \sum_j^N 2r_j r_p/(r_o - r_i)H}. \tag{9}$$

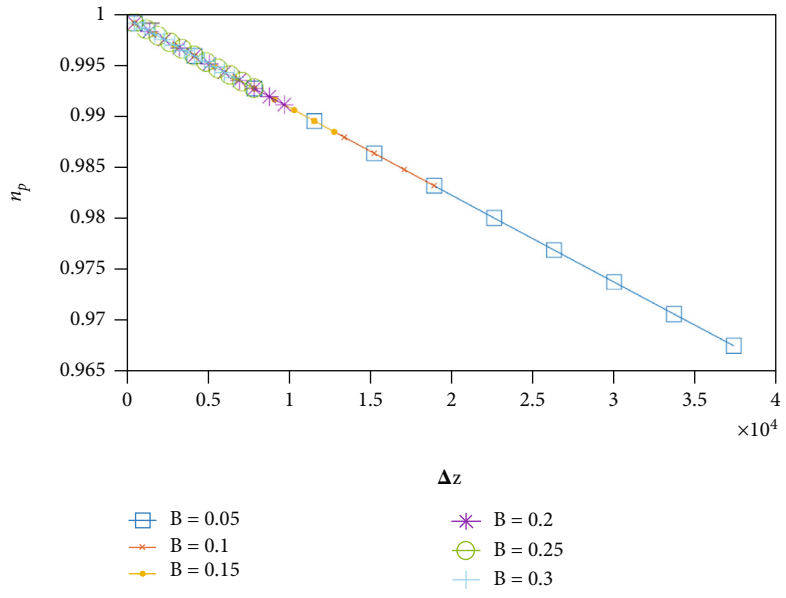

(a) Under different magnetic induction intensity

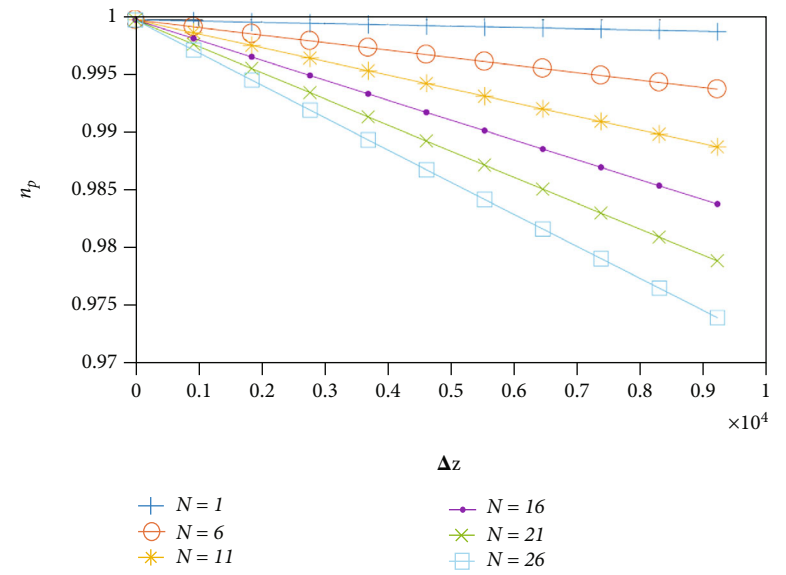

(b) Under different numbers of permanent magnets

Figure 5: Continued.

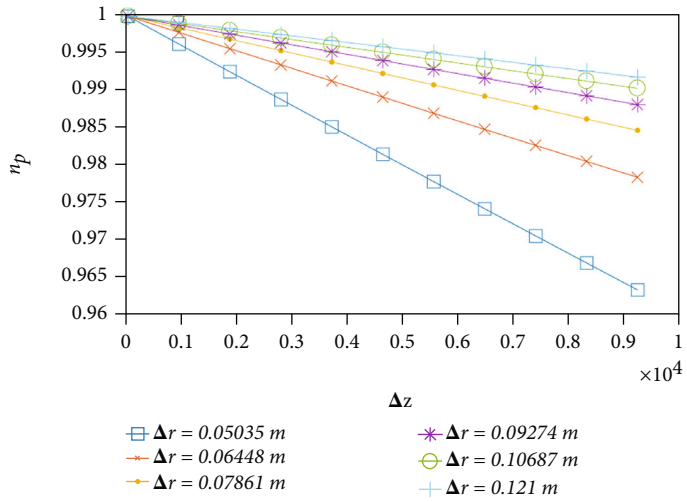

(c) Under different channel widths

Figure 5: Variation of primary electron density under different parameters.

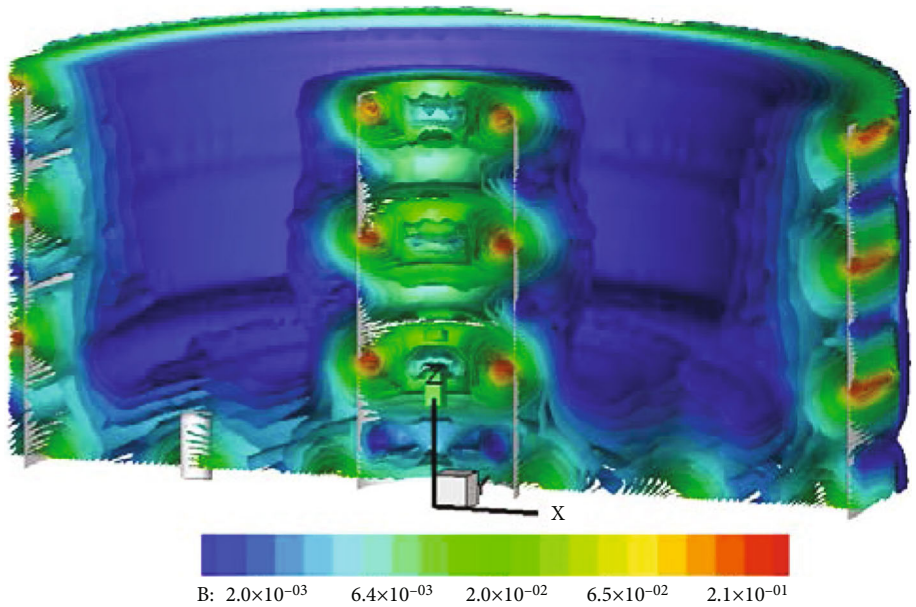

Figure 6: The designed magnetic field for an annular ion thruster (T).

To ensure the normal operation of the ion optics, the difference of plasma density upstream of the ion optics should not exceed one order of magnitude, that is, less than 10%. Therefore, here, we mainly focus on the circumferential decay degree of primary electron density, and n_p^0 is set to be 1. Then, four factors affect the circumferential distribution of primary electrons: the number of magnets, the difference between inner and outer radius, the height, and the magnetic field strength.

Let $\Delta r = r_o - r_i$ and $B = \|B\|$. Then, the simulation cases and their parameter settings are presented in Appendix A. Table 2 summarizes the values of input parameters for the analysis of circumferential distribution characteristics of primary electrons. Figure 3 shows the circumferential distribution of primary electrons of each case group.

According to the criterion (not less than 10%) and the results in Figure 3, it can be found that the circumferential distribution of primary electrons has the following characteristics: (1) it is sensitive to the magnetic field and changes nonlinearly. The magnetic field near the anode should be greater than 0.1 T. The stronger the magnetic field is, the better, but the improvement is not obvious when the magnetic field is greater than 0.2 T. (2) It is not sensitive to the number of magnets and changes almost linearly. The less the number of magnets is, the better. (3) It is also sensitive to the channel spacing and changes nonlinearly as well. The channel spacing should be greater than 0.06445 m, the wider the channel is, the better. But when the channel spacing is greater than 0.07861 m, the improvement is not obvious. (4) It is very insensitive to height.

Table 4: The reference parameters and the value.

Reference parameter	Value
Electronic mass, $m_{\text{ref}} = m_e$	9.3×10^{-31}kg
Elementary charge quantity, $q_{\text{ref}} = q_e$	1.602×10^{-19}
Vacuum dielectric constant, $\varepsilon_{\text{ref}} = \varepsilon_0$	8.85×10^{-12}Fm
Reference number density, n_{ref}	$1 \times 10^{18}\text{m}^{-3}$
Reference temperature, T_{ref}	5eV
Reference potential, Φ_{ref}	$\Phi_{\text{ref}} = kT_e/q_{\text{ref}}$
Reference length, L_{ref}	5×10^{-3}m
Reciprocal of electron cyclotron frequency, $t_{\text{ref}} = 1/\omega_e$ ω	$1/\omega_e = m_e/q_{\text{ref}}B_{\max}$
Electron sound velocity, $v_{\text{ref}} = v_s$	$v_s = \sqrt{kT_e/m_e}$
Reference electric field strength, E_{ref}	$E_{\text{ref}} = \Phi_{\text{ref}}/L_{\text{ref}}$
Reference magnetic induction, B_{ref}	$B_{\text{ref}} = B_{\max}$

Table 5: The normalized geometric parameters.

Parameter	Value
Outer anode diameter r_o	7.5
Height of outer anode	36
Inner anode diameter r_i	22.5
Height of inner anode	36
Radius of cathode	2
Height of cathode	6

2.1.2. Axial Distribution Characteristics of Primary Electrons. The axial transport characteristics of primary electrons are shown in Figure 4. Similarly, the axial distribution of primary electrons can be expressed as

$$\frac{d\left(n_p u_p^z\right)}{dz} A_s = -\frac{I_p}{q_p A_p} \sum_i^N L_m^i, \tag{10}$$

where L_m^i is the i_{th} magnet circumference; u_p^z is the axial diffusion velocity of primary electrons; A_s is the area of ion optics, and

$$A_s = \pi\left(r_o^2 - r_i^2\right). \tag{11}$$

Assuming that u_p^z is constant and $u_p^z = v_p$, then, we can get

$$\frac{dn_p}{dz} = -n_p \frac{\sum_i^N L_m^i}{A_s}. \tag{12}$$

Since the primary electrons are mainly lost at the magnetic tip, the loss length of the primary electron is discrete in the axial direction, that is, dz should be expressed as Δz, and

$$\Delta z = \sum_i^k 2r_p, k = 1 \cdots N. \tag{13}$$

Then, we can get

$$n_p = n_p^0 e^{-\Delta z \sum_i^N L_m^i / A_s}. \tag{14}$$

In Appendix A, Table 3 summarizes the values of input parameters for the analysis of axial distribution characteristics of primary electrons. Figure 5 shows the axial distribution of primary electrons of each case group. It indicates that the decay of the primary electron density in the axial direction is not obvious and is not sensitive to the number of magnets, the difference between inner and outer radius, and the magnetic field strength. Under all factors, the decay of the primary electron density in the axial direction is less than 10%.

2.2. Distribution Characteristics of Ions. In this section, we directly give the one-dimensional distribution equations of ions in the circumferential directions and then analyze their distribution characteristics. Note that because the loss of ions is mainly on the ion optics, and the loss on the anode can be negligible, the distribution of ions in the circumferential direction is only analyzed.

First, the circumferential distribution of ions can be expressed as

$$\frac{1}{r} \frac{d\left(n_i u_i^\theta\right)}{d\theta} = G_i - L_i, \tag{15}$$

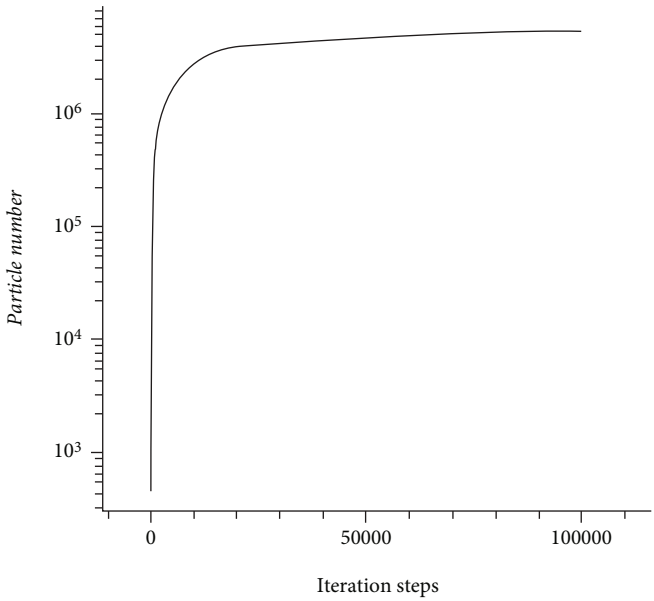

Figure 7: The curve of particle number with iteration steps.

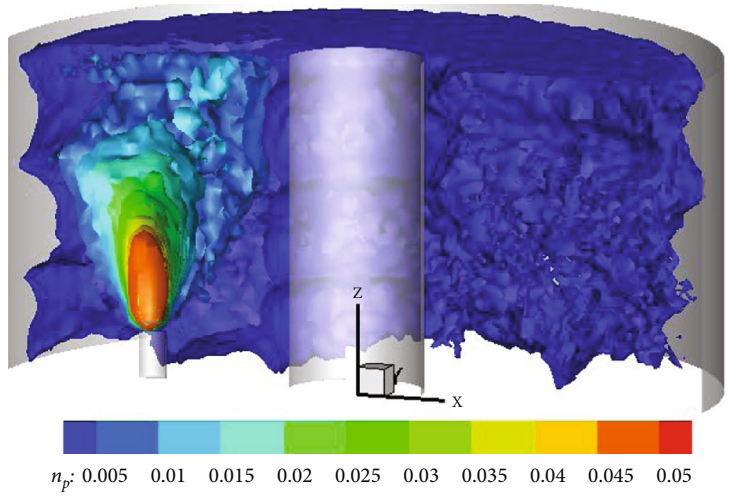

Figure 8: Distribution of primary electron density with the collision process.

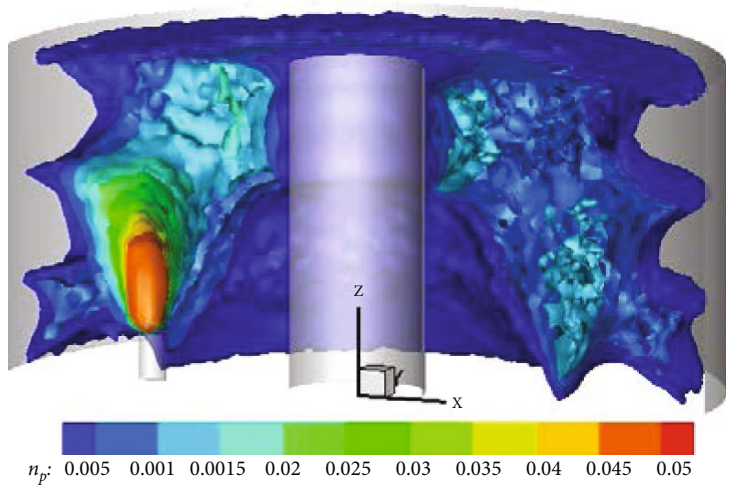

Figure 9: Distribution of primary electron density without the collision process.

where n_i is the ion density, u_i^θ is the circumferential diffusion velocity of ions, G_i is the production rate of ions, L_i is the loss rate of ions. Here, the production rate G_i of ions is assumed to be constant. The loss of ions on the anode is ignored, and the ion transmittance of ion optics is assumed to be 100%. Then, the loss rate L_i of ion is expressed as

$$L_i = \frac{I_i}{q_i A_s H}, \tag{16}$$

where q_i is the charge quantity of ions, I_i is the ion beam current, and

$$I_i = \frac{1}{2} n_i q_i \nu_{\text{Bohm}} A_s. \tag{17}$$

Suppose u_i^θ is also constant, hence

$$\frac{dn_i}{d\theta} = \frac{rG}{u_i^\theta} - \frac{1}{2} n_i \frac{r\nu_{\text{Bohm}}}{Hu_i^\theta}. \tag{18}$$

Finally, we can obtain the circumferential distribution of ions as follows

$$n_i = n_i^0 e^{-\theta r \nu_{\text{Bohm}}/2Hu_i^\theta} + \frac{2HG_i}{\nu_{\text{Bohm}}}. \tag{19}$$

Since the variables r, ν_{Bohm}, H, u_i^θ, are in the same order of magnitude, one can calculate that $e^{-\pi r \nu_{\text{Bohm}}/2Hu_i^\theta} \ll 0.9$ based on the values listed in Tables 2 and 3. Furthermore, since n_i^0 is very small, usually equal to 0, the distribution of ions is mainly determined by G_i, that is, the distribution of

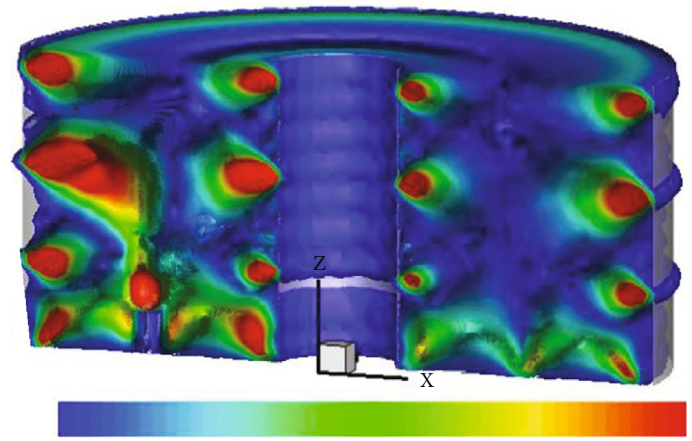

Bohm: 0.01 0.05 0.09 0.13 0.17 0.21 0.25 0.29 0.33 0.37 0.41 0.45 0.49

(a) Bohm collision

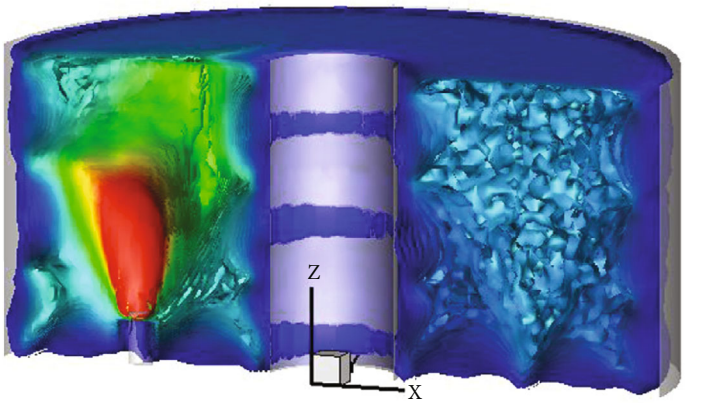

Elastic: 0.01 0.05 0.09 0.13 0.17 0.21 0.25 0.29 0.33 0.37 0.41 0.45 0.49

(b) Elasticity collision

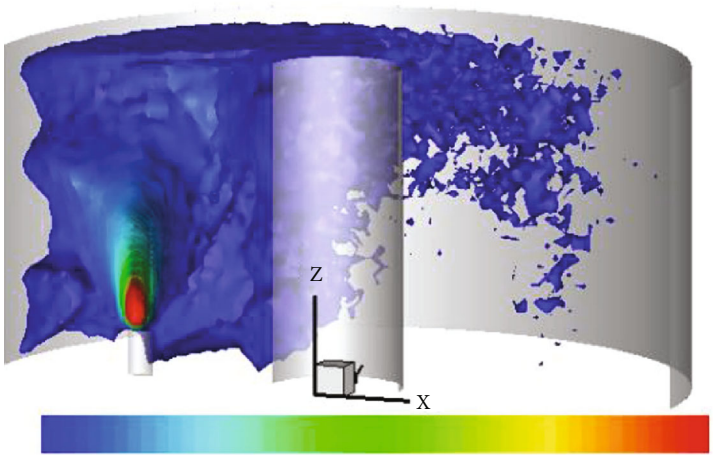

Excite: 0.01 0.05 0.09 0.13 0.17 0.21 0.25 0.29 0.33 0.37 0.41 0.45 0.49

(c) Excitation collision

Figure 10: Continued.

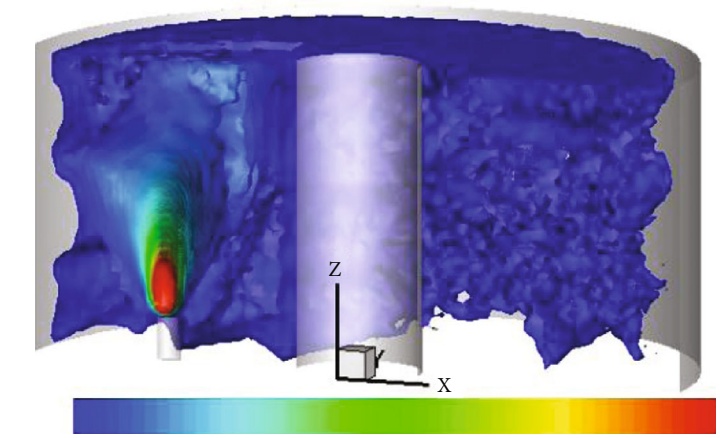

(d) Ionization collision

Figure 10: Distribution of Bohm, elasticity, excitation, and ionization collision.

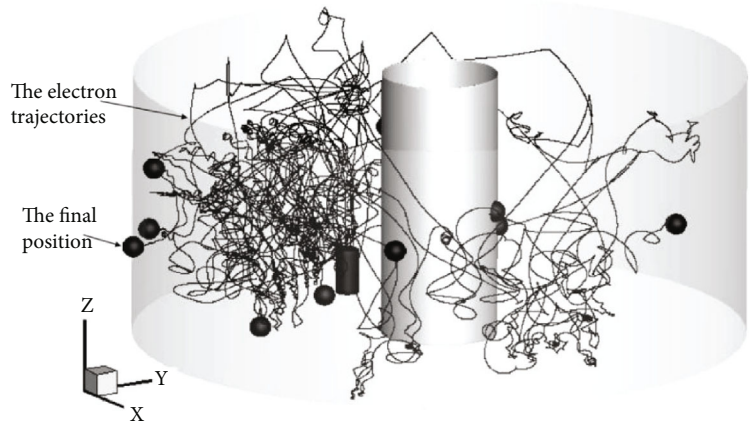

Figure 11: Primary electron trajectories.

ions mainly depends on the distribution of primary electrons but not on the diffusion process. Therefore, once the uniformly distributed primary electrons are obtained, the uniformly distributed ions will also be obtained.

2.3. The Design of Two Dimensional Magnetic Field Configuration Based on Theoretical Analysis. Based on the above results, we propose the design criteria of the two-dimensional magnetic field configuration for annular ion thruster in this section. We also draw on the magnetic field design criteria of traditional Kaufman-type ion thrusters. In Ref. [18], Wirz and Goebel found that the magnetic confinement and overall performance of the plasma generally improve with the increase of the maximum closed profile, B_{cc}. The field line topology needs to be carefully designed to effectively utilize the primary electrons and ensure ideal beam flatness, low double ion content, and good performance. The B_{cc} must be high enough to restrict the primary electrons. The B_{cc} must be low enough to allow stable discharge of all desired discharge plasma densities. Finally, Wirz and Goebel proposed that B_{cc} should be around 0.2 T [18].

To ensure the circumferential uniformity of electrons and ions, the following criteria should be satisfied.

Rule 1: the magnetic field near the anode should be large enough to effectively constrain the primary electrons. However, in order to ensure a large enough ionization region (i.e., the region where the magnetic field is less than B_{cc} [18]), the magnetic field of the permanent magnet cannot be too large. Therefore, according to the results in Section 2.1 and Section 2.2, the value 0.2 T is chosen.

Rule 2: the number of magnets should be few enough. However, if the number is too few, it is difficult to form an ideal closed profile, B_{cc}. Therefore, the MAXWELL 3D software [19] is used to simulate the magnetic field formed by different numbers of magnets. The results show that the minimum number of permanent magnets that can form an ideal closed profile is 9.

Rule 3: the channel spacing should be large enough. The designed maximum value 0.121 m is selected.

Rule 4: similar to rule 2, if the height is too high, it is difficult for the permanent magnets to form an ideal closed profile. Hence, the height should not be too large. Here, the designed minimum height 0.168 m is selected.

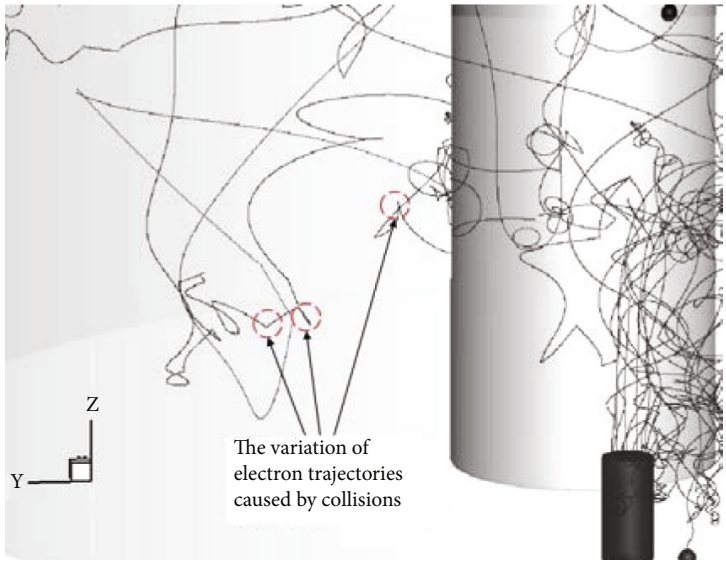

Figure 12: Primary electron trajectories near the anode (local).

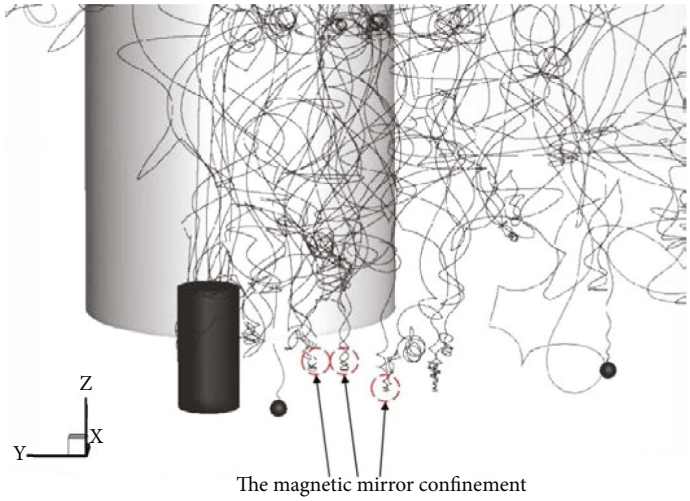

Figure 13: Primary electron trajectories near the cathode (local).

Based on the above criteria, a two-dimensional magnetic field configuration for the annular ion thruster is designed. Figure 6 shows the simulation results of the designed magnetic field, which is implemented through the MAXWELL 3D software [19]. In the next section, the limitations of two-dimensional magnetic field will be analyzed numerically based on this magnetic field configuration.

3. Numerical Analysis on the Limitations of the 2D Magnetic Field Configuration

In this section, the characteristics of primary electrons under the designed two-dimensional magnetic field configuration are simulated. The simulation model for the primary electrons is part of a 3D discharge chamber model for conventional Kaufman-type ion thrusters developed by Lu et al. [17, 20–23]. Then, the 3D density distribution, tangential average density distribution, different collision frequencies, and the traces of primary electron are presented. According to simulation results, the limitations of the 2D magnetic field structure are analyzed.

3.1. Computational Model. The model is built on the IFE-PIC-MCC method. In this paper, the PIC-MCC module is only used. In the PIC-MCC module, the plasma is set to be quasineutral, so its self-consistent field is ignored. The model is described below.

3.1.1. The PIC Method. In the PIC method, the detailed information of the flow field is obtained by directly tracking the movement of a large number of simulated particles. First, the initial state of the simulated particle must be determined according to the input conditions. In this model, the initial states of the primary electrons include the injected number of each step, the initial position, and the initial velocity.

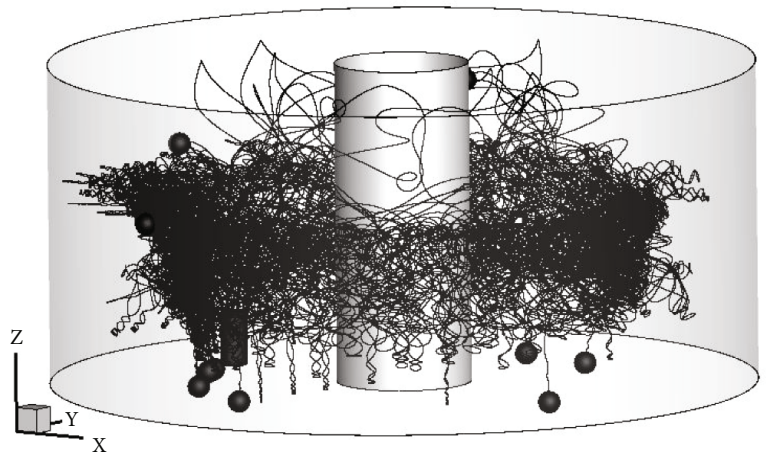

Figure 14: Primary electron trajectories without collision process.

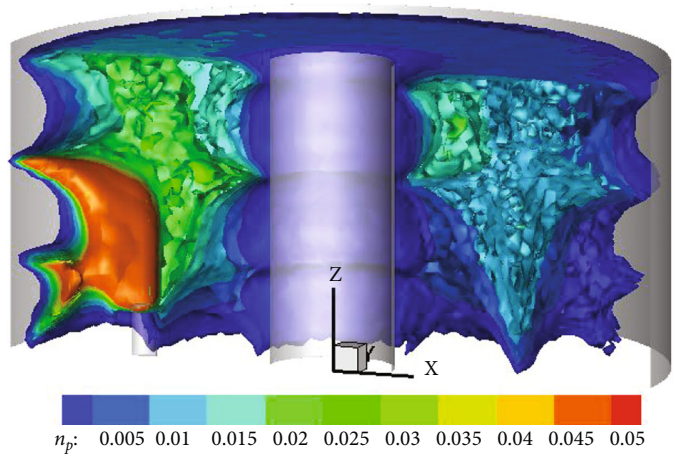

Figure 15: Distribution of primary electron density with 6 times the initial magnetic field strength.

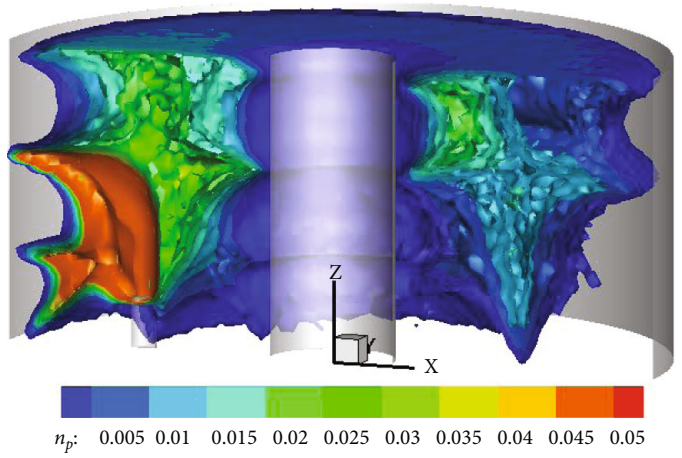

Figure 16: Distribution of primary electron density with 10 times the initial magnetic field strength.

The number and initial position can be determined by the emission current I_e and the position of the cathode top, while the initial velocity is determined by the initial energy of the primary electron.

I_e refers to the current emitted from the cathode, while the discharge current I_d refers to the current consisting of charged particles received from the anode, and beam current I_b refers to the current consisting of ions drawn from the

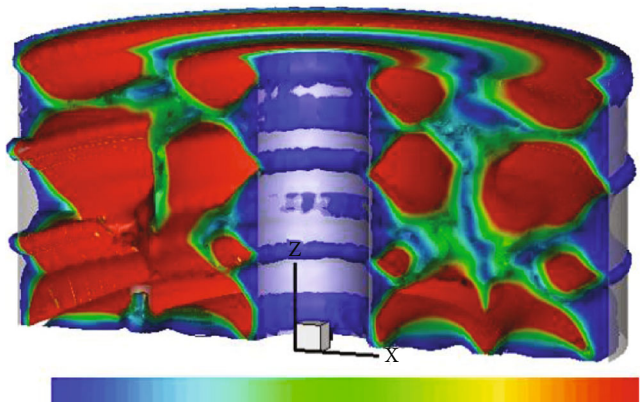

Bohm: 0.01 0.05 0.09 0.13 0.17 0.21 0.25 0.29 0.33 0.37 0.41 0.45 0.49

(a) Bohm collision

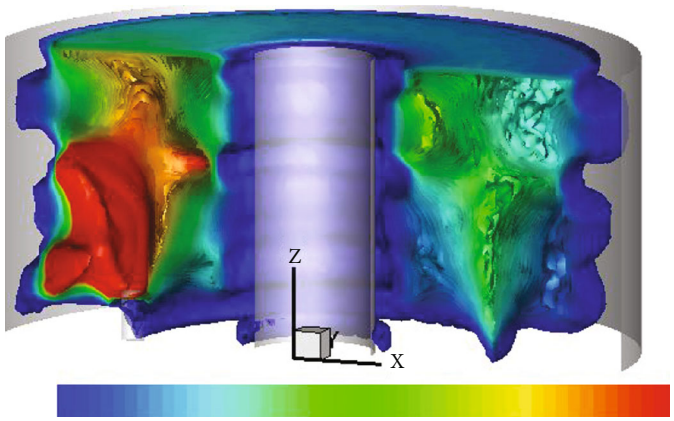

Elastic: 0.01 0.05 0.09 0.13 0.17 0.21 0.25 0.29 0.33 0.37 0.41 0.45 0.49

(b) Elasticity collision

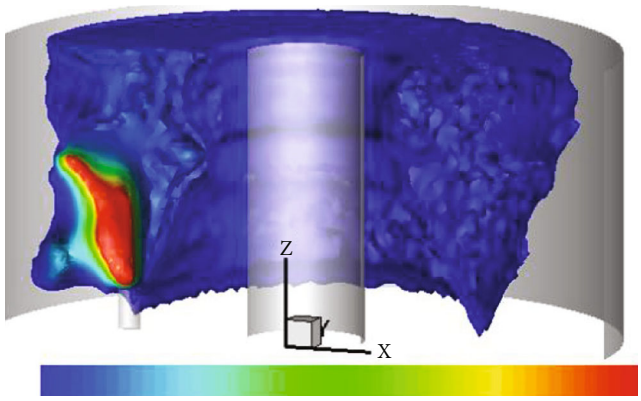

Excite: 0.01 0.05 0.09 0.13 0.17 0.21 0.25 0.29 0.33 0.37 0.41 0.45 0.49

(c) Excitation collision

Figure 17: Continued.

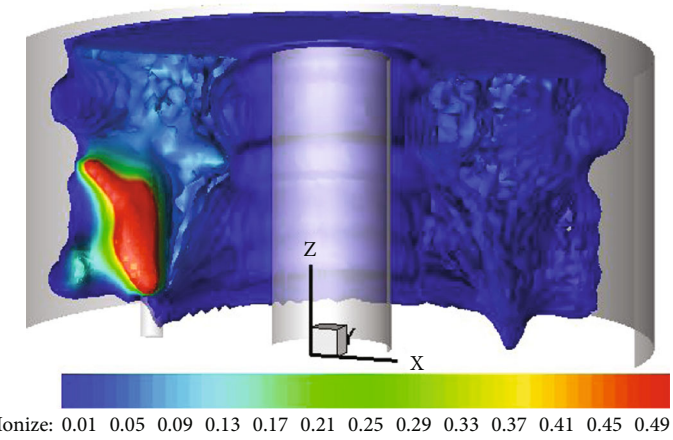

(d) Ionization collision

FIGURE 17: Distribution of Bohm, elasticity, excitation, and ionization collision with 6 times the initial magnetic field strength.

optics. In an ideal ion thruster discharge chamber, all ions are extracted by the optics, while all electrons (including primary electrons and secondary electrons) are absorbed by the anode. Therefore, the discharge current I_d is mainly composed of I_e and the secondary electron current I_{se}. The number of secondary electrons is equal to the number of ions, hence, $I_{se} = I_b$.

Therefore, I_{se} can be calculated from discharge current I_d and beam current I_b [23]:

$$I_e = I_d - I_b. \tag{20}$$

The initial position of the primary electrons is located at the cathode emitter, and the primary electrons are uniformly distributed. In addition, the sheath thickness at each boundary of the discharge chamber is neglected, hence, the primary electrons are assumed to emit from the cathode sheath edge. Therefore, the initial velocity of the primary electron is the velocity accelerated by the cathode sheath potential. Since the potential drop of the cathode sheath (about 30 V) is much larger than the thermal kinetic energy of the primary electron (about 2 eV), the initial velocity of the primary electron in the axial direction (Z-direction) is defined as the velocity accelerated by the cathode sheath potential, while the initial velocity in the other two directions (X and Y direction) conforms to Maxwell distribution [23]:

$$u_p = \begin{cases} u_{px} = v_{th}\sqrt{-\ln(R)}\,\sin(2\pi R), \\ u_{py} = v_{th}\sqrt{-\ln(R)}\,\cos(2\pi R), \\ u_{pz} = \sqrt{\dfrac{2q\phi_c}{m_p}}, \end{cases} \tag{21}$$

where v_{th} is the most probable thermal velocity, R is a random number between 0 and 1, and ϕ_c is the potential drop of cathode sheath. Then, the trajectory of primary electrons is determined by Newton's second law and Lorentz force:

$$m_p \frac{du_p}{dt} = q_p\left(E + u_p \times B\right). \tag{22}$$

The above equation is solved by Boris's leaping frog algorithm [24]. If primary electrons impact the cathode or the screen grid, they are reflected into the discharge chamber, and the reflection is taken as being specular [25], while, if they impact the anode, they are considered to be absorbed. In addition, if the energy of a primary electron is less than the threshold of ionization collision, it will be also deleted from the simulation domain [25]. The time step for the primary electrons is one-third of the primary electron cyclotron frequency.

3.1.2. The MCC Method. In the MCC method, only four collision types of primary electrons are considered: elastic collision, excitation collision, ionization collision, and Bohm collision [26] When all of these collisions occur, it is assumed that the neutral atoms remain unchanged. If elastic collisions occur, the energy of primary electrons remains unchanged, but the velocity will be reset; if an excitation collision occurs, the primary electron loses 8.32 eV of energy, and then the velocity direction is reset again; if an ionization collision occurs, the energy of both the primary electron and the newly generated secondary electron needs to be restored, which conforms to the following function [26]:

$$f\left(\varepsilon_s, \varepsilon_p\right) = \frac{\vartheta\sigma_i}{\left(\vartheta^2 + \varepsilon_s^2\right)\arctan\left(\varepsilon_p - I/2\vartheta\right)}, \tag{23}$$

where ε_s is the energy of newly generated secondary electrons; ε_p is the energy of the primary electrons after ionization; ϑ is the ionization parameter with a value of 8.7 eV; I is the threshold of ionization energy; σ_i is the cross section of ionization collision.

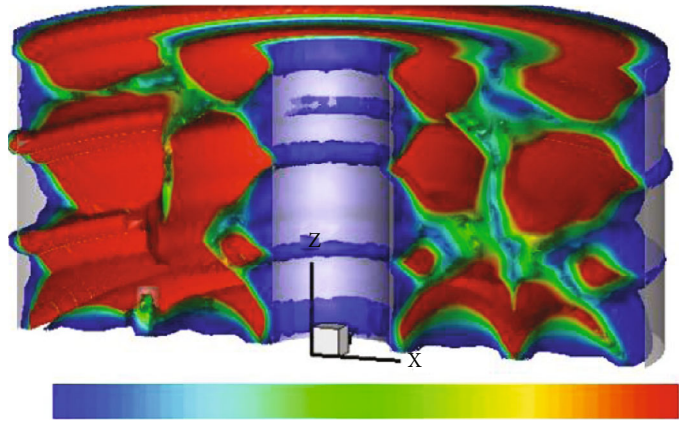

Bohm: 0.01 0.05 0.09 0.13 0.17 0.21 0.25 0.29 0.33 0.37 0.41 0.45 0.49

(a) Bohm collision

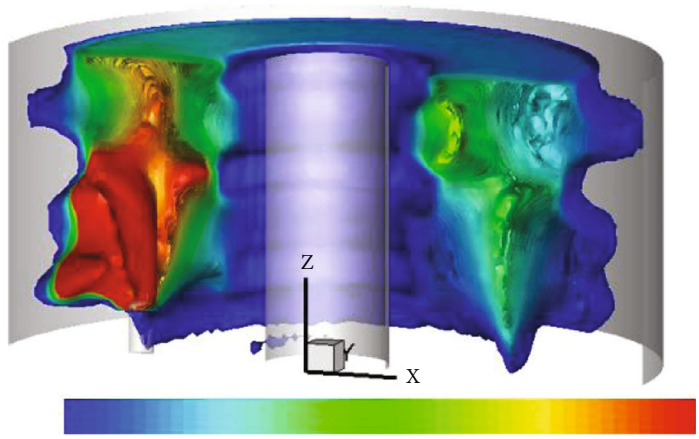

Elastic: 0.01 0.05 0.09 0.13 0.17 0.21 0.25 0.29 0.33 0.37 0.41 0.45 0.49

(b) Elasticity collision

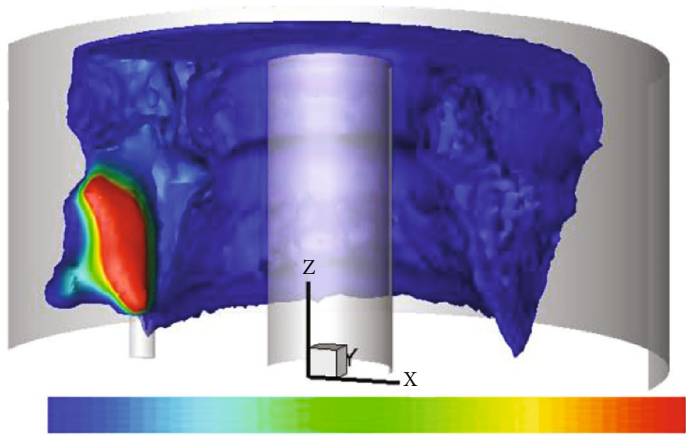

Excite: 0.01 0.05 0.09 0.13 0.17 0.21 0.25 0.29 0.33 0.37 0.41 0.45 0.49

(c) Excitation collision

Figure 18: Continued.

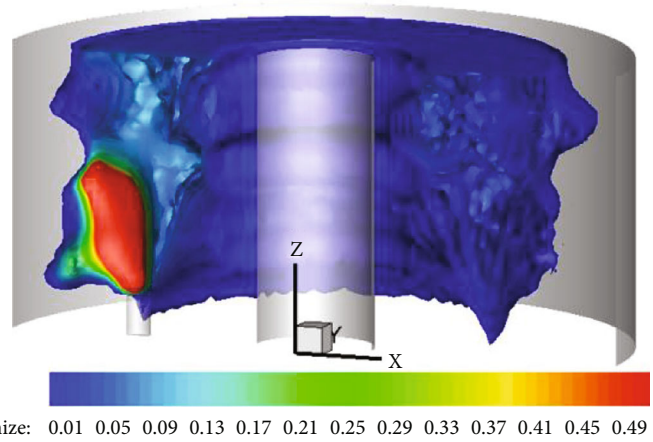

(d) Ionization collision

Figure 18: Distribution of Bohm, elasticity, excitation, and ionization collision with 10 times the initial magnetic field strength.

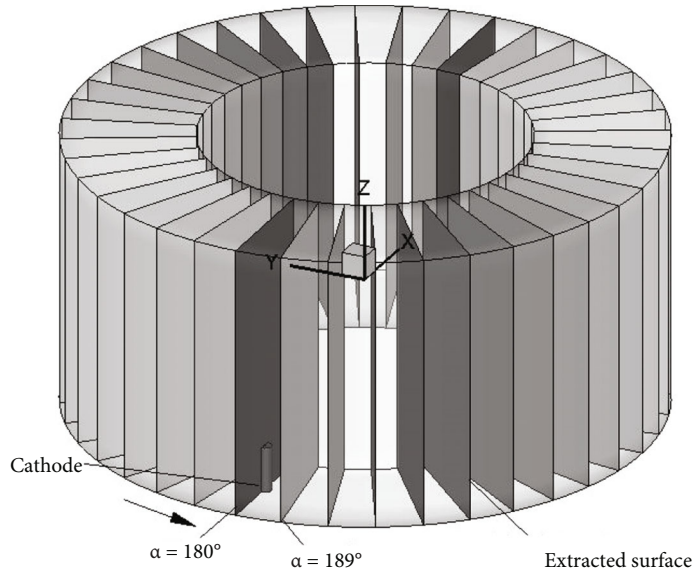

Figure 19: Diagram of section.

The collision frequencies of elastic collision ν_{elastic}, excitation collision ν_{excite}, ionization collision $\nu_{\text{ionization}}$, and Bohm collision [27] ν_{Bohm} are

$$\begin{aligned} \nu_{\text{ionnization}} &= \sigma_i \rho_0 \left\| u_p \right\|, \\ \nu_{\text{elastic}} &= \sigma_{el} \rho_0 \left\| u_p \right\|, \\ \nu_{\text{excite}} &= \sigma_{ex} \rho_0 \left\| u_p \right\|, \\ \nu_{\text{Bohm}} &= \frac{1}{64} \frac{q_p \|B\|}{m_p}, \end{aligned} \tag{24}$$

where $\sigma_i, \sigma_{el}, \sigma_{ex}$ are the collision cross sections of elastic collision, excitation collision, and ionization collision, respectively (the values of each collision cross section can be referred to Ref. [28]). $\|u_p\|$ and $\|B\|$ represent the modes of the primary electron velocity and magnetic induction intensity, respectively, that is, $\|u_p\| = \sqrt{u_{px}^2 + u_{py}^2 + u_{pz}^2}$ and $\|B\| = \sqrt{B_x^2 + B_y^2 + B_z^2}$.

Furthermore, in the MCC method, the null collision method [28] is introduced. First, the maximum collision probability $P_{\max}$ is calculated in each step

$$P_{\max} = 1 - \exp\left(-\nu_{\max} dt\right), \tag{25}$$

where $\nu_{\max}$ is the maximum collision frequency, $\nu_{\max} = \max(\sigma) \cdot \max(u_p)$.

Second, $P_{\max}$ is compared with a random number R_1. If $R_1 < P_{\max}$, some collision is considered to have happened. Then, another random number R_2 is generated to determine what kind of collision occurs. If $R_2 < \nu_1/\nu_{tot}$, where ν_{tot} is the total collision frequency and $\nu_{tot} = \sum_{j=1}^{4} \nu_j$, the first collision

will occur; if $v_1/v_{tot} < R_2 < (v_1 + v_2)/v_{tot}$, the second collision will occur, and so on. If $R_1 > P_{\max}$, no collision is considered.

3.2. Simulation Setup. In our model, atoms are set to be a uniformly distributed background, and their number density is set to be 1.86×10^{-6}. Discharge currents and beam currents are 11 A and 1 A, respectively. Hence, the cathode emission current is set to be 10 A. The plasma is assumed to be quasi with equal potential, so the electric field in the discharge chamber is ignored. Due to ignoring the plasma self-consistent electric field, a large mesh length is chosen, which is set to 5×10^{-5} m. The time step is set to be less than one-third of the reciprocal of electron cyclotron frequency, which is about 10^{-11} s. The reference parameters and the reference values of these parameters are shown in Table 4. In the following content, except for the results marked with units, the rest of the simulation results are all normalized results. Table 5 shows its initial normalized geometric parameters. The whole normalized simulation domain is set to $83 \times 83 \times 36$. For each case, the time required for the PIC-MCC loop to reach the steady-state is about 6 hours on a 2.8 GHz HP Z620 workstation.

3.3. Simulation Results and Analysis. Here, we analyze the limitations of the two-dimensional magnetic field configuration by the distribution characteristics of the primary electrons, their trajectories, magnetic field streamlines, and the distribution characteristics of various collision frequencies. The results of numerical examples with and without collisions, as well as with different magnetic field intensities, are mainly compared and studied.

3.3.1. Influence of Collision Process on Magnetic Confinement. First, to show the convergence of our method, Figure 7 presents the curve of particle number with iteration steps. It shows that when the number of iteration steps exceeds 100000, the calculation converges.

Figure 8 presents the number density of primary electrons with the collision process. Obviously, the density at the cathode side is much higher than that of the other side. The density of primary electrons upstream of the ion optics on the cathode axis is about 10 times higher than that of the other side. The density of primary electrons is nonaxisymmetric. Another obvious feature is that, because of the mirror effect, electrons form a sharp cone near the anode.

Figure 9 shows the number density of primary electrons without the collision process. Compared with Figure 8, the distribution of primary electrons in Figure 9 is more concentrated in the discharge channel. The density of primary electrons upstream of the ion optics on the cathode axis is about 3 times higher than that of the other side. This means that, without the collision process, the circumferential distribution of primary electrons is more uniform.

Figure 10 shows the distribution of Bohm, elasticity, excitation, and ionization collision frequencies. It can be found that, in all of these four collisions, Bohm collision and elastic collision are dominant.

Figure 11 shows the primary electron trajectories. The trajectory shows that the primary electrons only move locally at the cathode and rarely move to the opposite side of the cathode.

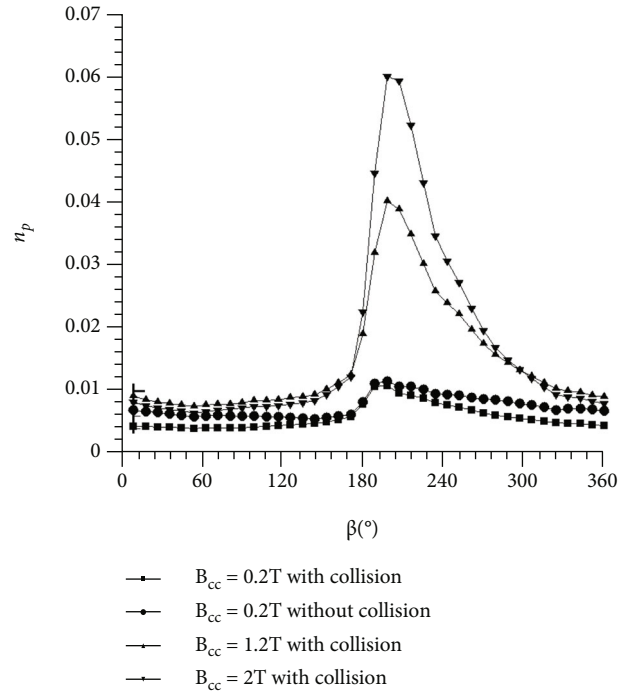

Figure 20: The change of primary electron density along the circumferential direction.

Figures 12 and 13 show the primary electron trajectories in local regions. An obvious magnetic mirror effect was observed near the cathode. In the channel far away from the cathode, the collision process was observed.

Figure 14 shows the primary electron trajectories without collision process. The trajectory shows that the primary electrons have obvious circumferential movement. The above results show that the atom forms significant impedance to the circumferential motion of the primary electron. Without the collision process, the primary electrons can form obvious circumferential motion under the confinement of the magnetic mirror. The primary electron circumferential distribution is close to the theoretical prediction in the previous section. However, when the collision process is considered, the primary electrons only move locally at the cathode. The primary electron circumferential distribution deviates far from the theoretical prediction in the previous section.

3.3.2. Limitations of the Two-Dimensional Magnetic Field Configuration. Figures 15 and 16 show the number density of primary electrons under 6 and 10 times the initial magnetic field strength, respectively. With the increase of magnetic field intensity, the density of primary electrons in the channel increases significantly. The distribution of primary electrons in Figures 14 and 15 are also more concentrated in the discharge channel. This means that the confinement of the magnetic field to the primary electron is strengthened. However, the densities of primary electrons upstream of the

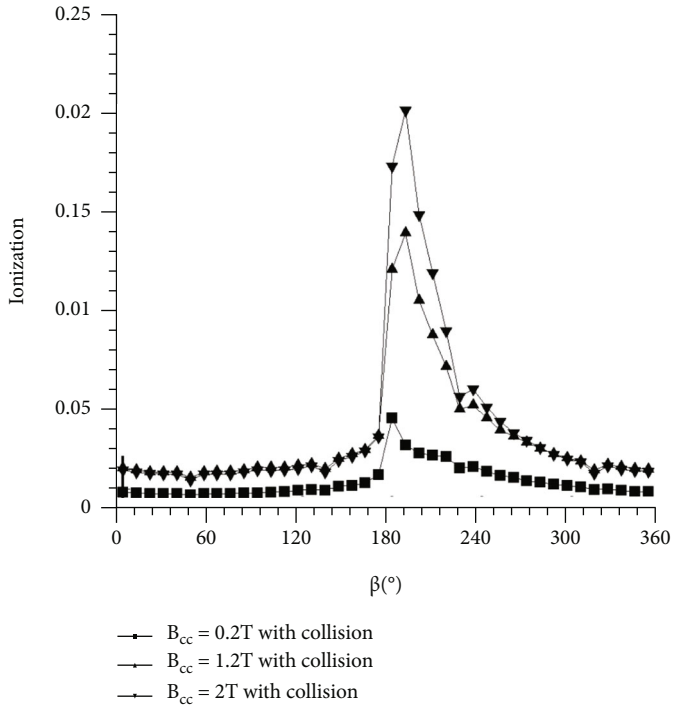

Figure 21: The change of ionization rate along the circumferential direction.

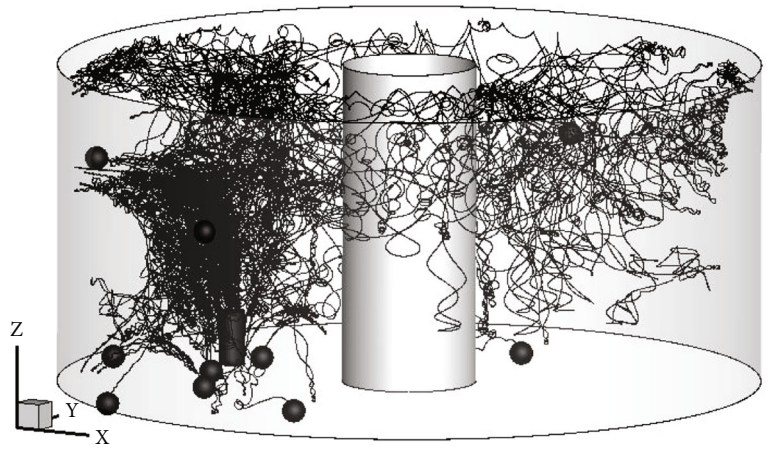

Figure 22: Primary electron trajectories under 6 times the initial magnetic field strength.

ion optics on the cathode axis are about 40 and 60 times higher than that of the other side, respectively.

Figures 17 and 18 show the collision rate distribution under 6 and 10 times the initial magnetic field strength, respectively. Obviously, with the increase of magnetic field strength, the primary electron density increases, and the frequency of all kinds of collisions also increases.

To show the above difference more clearly, we extract 40 surfaces in the discharge chamber and calculate the average density on each surface. The extracted surfaces are shown in Figure 19. The angle of the surface cutting the cathode around the thruster axis is set to be $\alpha = 180^{\circ}$, where the counterclockwise direction is set to the rotation direction. Figure 20 presents the average ionization rate of each case, and Figure 21 presents the average ionization rate of each case. The results show that, when the collision process is not considered, the circumferential distribution of primary electrons is the most uniform. However, increasing the magnetic field intensity does not improve the uniformity of the primary electron circumferential distribution, but aggravates the nonuniformity.

Figures 22 and 23 present the primary electron trajectories under 6 and 10 times the initial magnetic field strength, respectively. They show that with the increase of magnetic field strength, a large number of primary electrons only move locally near the cathode.

Figure 24 presents the local magnetic field lines near the cathode. Figure 25 presents the 3D views of magnetic field

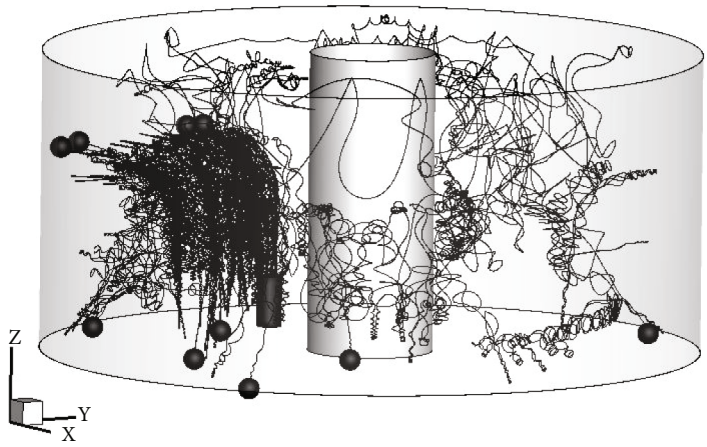

Figure 23: Primary electron trajectories under 10 times the initial magnetic field strength.

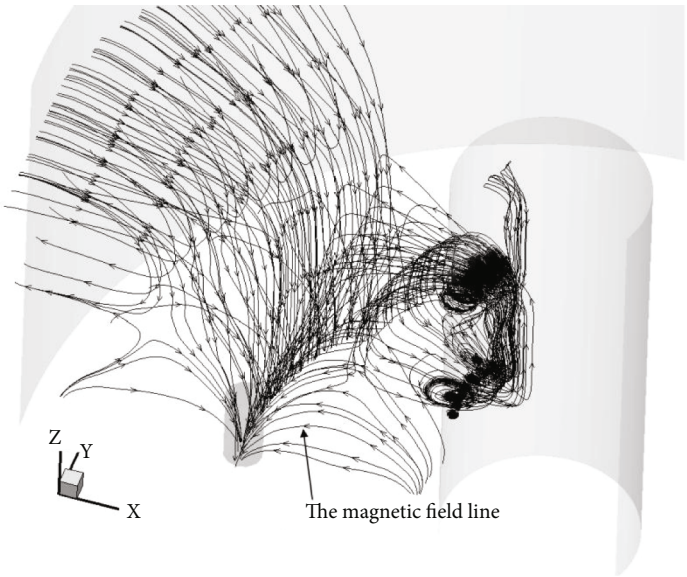

Figure 24: 3D view of magnetic field line near cathode.

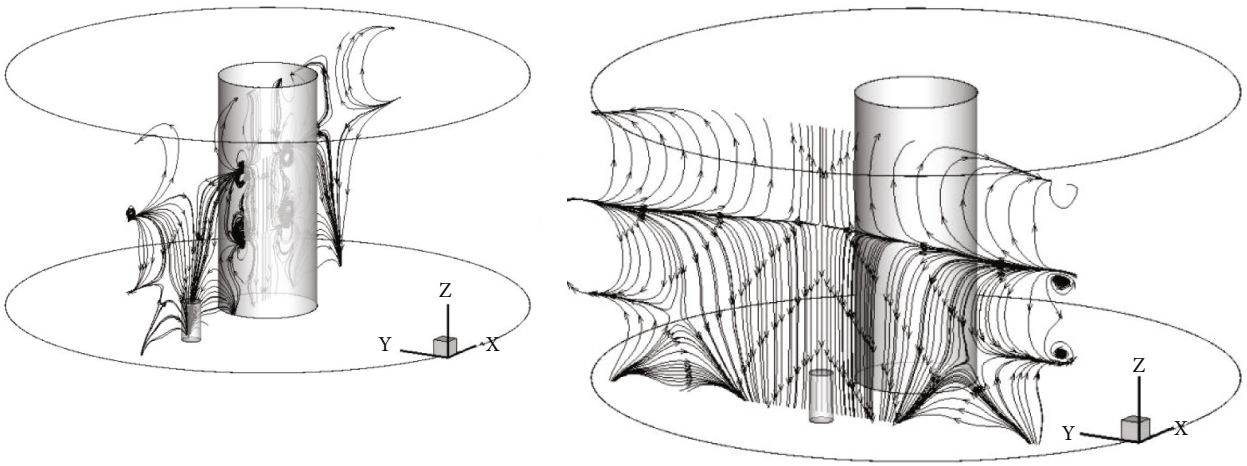

(a) *XZ* section (b) *YZ* section

Figure 25: Different sections of 3D view of magnetic field line near cathode.

line near cathode at XZ section and YZ section, respectively. It can be seen from the figure that the magnetic field of the two-dimensional configuration cannot guide and constrain the motion of the primary electron in the circumferential direction. Therefore, when the magnetic field intensity increases, more primary electrons will be constrained to move only locally at the cathode.

4. Conclusions

In this paper, the confinement characteristics of primary electrons and ions in an annular ion thruster with the two-dimensional magnetic field configuration are first analyzed theoretically. Then, according to the analysis, a two-dimensional magnetic field configuration for the annular ion thruster is designed. On this basis, the limitations of the two-dimensional magnetic field structure are analyzed and discussed by a three-dimensional (3D) Particle-in-cell Monte Carlo collision (PIC- MCC) model. The results show that:

(1) Both the simulation results and theoretical analysis results show that, only when the collision process is not considered, the primary electrons can be well constrained by the two-dimensional magnetic field. Hence, only in this ideal situation, a uniform distribution of primary electrons can be achieved

(2) When considering the collision process, the atom forms a significant impedance to the circumferential motion of the primary electron. Meanwhile, the collision process greatly increases the loss rate of primary electrons and aggravates the nonuniformity, causing that the simulation results are far worse than the theoretical analysis results

(3) Because the primary electron lacks guidance and constraint in the circumferential direction under the two-dimensional magnetic field configuration, the uniformity of discharge cannot be improved only by increasing the magnetic field intensity

Finally, to sum up, the circumferential constraint on charged particles must be considered for the magnetic field configuration of annular ion thruster. This will be an important research direction of annular ion thruster in the future.

Appendix

A. Parameter Settings for the Theoretical Analysis

The value of each parameter is referred to Ref. [12]. Table 2 summarizes the values of input parameters for the analysis of circumferential distribution characteristics of primary electrons, and 4 case groups are set, i.e., case groups 1-4. In case group 1, 6 different values of B are set; in case group 2, 6 different values of N are set; in case group 3, 6 different values of Δr are set; in case group 4, 6 different values of H are set. The calculation results of case groups 1-4 are shown in Figure 3.

Table 3 summarizes the values of input parameters for the analysis of axis distribution characteristics of primary electrons, and 3 case groups are set, i.e., case groups 5-7. In case group 5, 6 different values of B are set; in case group 6, 6 different values of N are set; in case group 7, 6 different values of Δr are set. The calculation results of case groups 5-7 are shown in Figure 5.

Data Availability

Some or all data, models, or code generated or used during the study are available from the corresponding author by request.

Conflicts of Interest

The authors declare that they have no conflicts of interest.

Acknowledgments

This work was supported by the National Key R & D Program of China (no. 2020YFC2201100), the National Natural Science Foundation of China (nos. 12102082 and 12175032), the National Key R & D Program for Intergovernmental International Scientific and Technological Innovation Cooperation (no. 2021YFE0116000), the Fundamental Research Funds for the Central Universities of China (no. DUT21GJ206), Key Research and Development Project of Liaoning Province (no. 2020JH2/10500003), and the Central Guided Local Science and Technology Development Project (no. 216Z1901G).

References

[1] C. Cai, "Numerical studies on plasma plume flows from a cluster of electric propulsion devices," *Aerospace Science and Technology*, vol. 41, pp. 134–143, 2015.

[2] J. Kindracki, P. Paszkiewicz, and L. Mezyk, "Resistojet thruster with supercapacitor power source - design and experimental research," *Aerospace Science and Technology*, vol. 92, pp. 847–857, 2019.

[3] I. Levchenko, O. Baranov, J. Fang, O. Cherkun, S. Xu, and K. Bazaka, "Focusing plasma jets to achieve high current density: feasibility and opportunities for applications in debris removal and space exploration," *Aerospace Science and Technology*, vol. 108, article 106343, 2021.

[4] Z. Zhe, Z. Zun, X. Shuting, L. L. William Yeong, R. Junxue, and T. Haibin, "Three dimensional measurement of a stationary plasma plume with a faraday probe array," *Aerospace Science and Technology*, vol. 110, article 106480, 2021.

[5] Y. Cheng and G. Xia, "Investigation into the transient flow characteristics of noble gas propellants using the pulsed inductive discharge in electric propulsion," *Chinese Journal of Aeronautics*, vol. 33, no. 9, pp. 2329–2341, 2020.

[6] T. Wang, "Collision avoidance of coulomb spacecraft formations using multi-mode hall thrusters," *Aerospace Science and Technology*, vol. 68, pp. 261–268, 2017.

[7] Y. Cheng and G. Xia, "Simulation of plasma behavior for medium propellant mass and pulsed energy of small scale pulsed inductive thruster," *Chinese Journal of Aeronautics*, vol. 33, no. 1, pp. 176–190, 2020.

[8] M. Patterson and R. S. D. Herman, "Annular-geometry ion engine: concept, development status, and preliminary performance," in *48th AIAA/ASME/SAE/ASEE Joint Propulsion Conference & Exhibit*, 2012.

[9] G. Aston, M. B. Aston, and J. B. Kolts, "Preliminary tests of annular ion optics," in *28th AIAA/ASME/SAE/ASEE Joint Propulsion Conference & Exhibit*, 1992.

[10] G. Aston, M. B. Aston, and V. K. Rawlin, "50cm ion engine operation with annular ion accelerator system," in *31st AIAA/ASME/SAE/ASEE Joint Propulsion Conference & Exhibit*, 1995.

[11] G. Aston and J. R. Brophy, "A 50cm diameter annular ion engine," in *25th A-IAA/ASME/SAE/ASEE Joint Propulsion Conference & Exhibit*, 1989.

[12] J. Chen, T. Zhang, M. Liu, Z. Gu, W. Yang, and L. Yang, "Modeling and simulation of the effect of cathode gas flow on the lifetime and performance of an annular-geometry ion engine," *IEEE Transactions on Plasma Science*, vol. 47, no. 1, pp. 357–364, 2019.

[13] M. Patterson, "Next-generation electric propulsion thrusters," in *47th Joint Propulsion Conference*, 2011.

[14] R. Shastry, M. J. Patterson, and D. A. Herman, "Current density measurements of an annular- geometry ion engine," in *48th AIAA/ASME/SAE/ASEE Joint Propulsion Conference & Exhibit*, 2012.

[15] M. J. Patterson, J. E. Foster, and J. A. Young, "Annular engine development status," in *48th AIAA/ASME/SAE/ASEE Joint Propulsion Conference & Exhibit*, 2013.

[16] H. Cao, Y. Chu, E. Wang, C. Yong, and Z. Zhang, "Numerical simulation study on barrel erosion of ion thruster accelerator grid," *Journal of Propulsion and Power*, vol. 31, no. 6, pp. 1785–1792, 2015.

[17] C. Lu, J. Wan, Y. Cao, and X. He, "A fully decoupled iterative method with three-dimensional anisotropic immersed finite elements for Kaufman-type discharge problems," *Computer Methods in Applied Mechanics and Engineering*, vol. 372, article 113345, 2020.

[18] R. Wirz and D. Goebel, "Effects of magnetic field topography on ion thruster discharge performance," *Plasma Sources Science and Technology*, vol. 17, no. 3, article 035010, 2008.

[19] A. Corporation, *Maxwell 3d Software Package, ver. 3.1.04*, Pittsburgh, PA, 2005.

[20] C. Lu, Z. Yang, J. Bai, Y. Cao, and X. He, "Three dimensional immersed finite element method for anisotropic magnetostatic electrostatic interface problems with nonhomogeneous flux jump," *International Journal for Numerical Methods in Engineering*, vol. 121, no. 10, pp. 2107–2127, 2020.

[21] C. Lu, T. Zhang, P. Qiu, J. Chen, Y. Cao, and L. Zheng, "Barrel erosion of ion thruster accelerator grid under different operating conditions," *IEEE Transactions on Plasma Science*, vol. 46, no. 12, pp. 4065–4077, 2018.

[22] C. Lu, Y. Zhao, J. Wan, Y. Chu, L. Zheng, and Y. Cao, "Influence of the decelerator grid on the optical performance of the ion thruster," *International journal of aerospace engineering*, vol. 2019, no. 2, p. 8916303.11, 2019.

[23] C. Lu, G. Q. Xia, B. Sun, and Y. J. Han, "Confinement characteristic of primary electrons with the variation of channel width in the discharge chamber of annular ion thruster," *Chinese Journal of Aeronautics*, vol. 34, no. 5, pp. 79–92, 2021.

[24] T. Ogunjobi and J. Menart, "Computational study of ring-cusp magnet configurations that provide maximum electron confinement," in *42nd AIAA/ASME/SAE/ASEE Joint Propulsion Conference & Exhibit*, 2006.

[25] R. Wirz, *Discharge Plasma Processes of Ring-Cusp Ion Thrusters*, California Institute of Technology, 2005.

[26] G. Xia, Y. Han, L. Chen, Y. Wei, Y. Yu, and M. Chen, "Simulations of momentum transfer process between solar wind plasma and bias voltage tethers of electric sail thruster," *Acta Astronautica*, vol. 147, no. JUN., pp. 107–113, 2018.

[27] J. J. Szabo, *Fully Kinetic Numerical Modeling of a Plasma Thruster*, Massachusetts Institute of Technology, 2001.

[28] V. Vahedi and M. Surendra, "A Monte Carlo collision model for the particle-in-cell method: applications to argon and oxygen discharges," *Computer Physics Communications*, vol. 87, no. 1-2, pp. 179–198, 1995.